Effect of ion irradiation of the metal matrix on the oxidation rate of Zircaloy-4

Marc Tupin, Romain Verlet, Kimberly Colas, Michael Jublot, Gérard Baldacchino, Krzysztof Wolski

Corrosion Science 136 (2018) 28–37

Contents lists available at ScienceDirect

Corrosion Science

journal homepage: www.elsevier.com/locate/corsci

Effect of ion irradiation of the metal matrix on the oxidation rate of Zircaloy-4

Marc Tupin[a,*], Romain Verlet[a,1], Kimberly Colas[a], Michael Jublot[a], Gérard Baldacchino[b], Krzysztof Wolski[c]

[a] CEA/DEN/Service d'Etude des Matériaux Irradiés, CEA/Saclay, Université Paris-Sacaly, 91191 Gif-sur-Yvette Cedex, France
[b] LIDYL, CEA, CNRS, Université Paris-Saclay, F-91191 Gif-sur-Yvette, France
[c] Ecole des Mines de Saint Etienne, Centre SMS, UMR5307, 158 cours Fauriel, 42023 Saint Etienne Cedex France

ARTICLE INFO

Keywords:
Zircaloy-4
Oxidation
Irradiation
SIMS
Reactor conditions

ABSTRACT

The oxidation kinetics acceleration observed in Zircaloy-4 cladding in Pressurized Water Reactor could be partially due to metal irradiation damage occuring in-pile. To check this assumption, several ion irradiation tests of the Zircaloy-4 metal matrix were performed to reproduce the evolution of the metallurgical state in reactor. This study showed that the amorphization process of the intermetallic precipitates (SPPs) does not change significantly the oxidation rate of Zircaloy-4. Implantation of iron in the matrix to simulate iron dissolution from the SPPs has no real impact on the corrosion kinetics. However proton irradiations at 350 °C producing < a > dislocation loops resulted in a significant increase in the oxidation rate.

1. Introduction

In Pressurized Water Reactors (PWR), zirconium alloys used as fuel cladding are immersed in primary water at around 300 °C and 155 bar containing 0.7–2.2 wt.ppm Li, 10–1200 wt.ppm B and around 25 cm^3 H_2/kg of water. In these conditions, corrosion processes occur and the oxidation kinetics of Zircaloy-4 (Zr-1.3Sn-0.2Fe-0.1Cr written Zy4 afterwards) show a drastic acceleration phase beyond a burnup of approximately 35 GWd/tU [1,2]. This burnup is usually reached after 3 or 4 cycles in PWR.

Four major assumptions are proposed in the literature in order to explain this acceleration [3,4]. The first one is the effect of zirconium hydrides precipitated beneath the metal/oxide interface resulting from the hydrogen uptake by the matrix [5–8]. Other authors suggest that the acceleration of corrosion is due to the evolution of the tin distribution during corrosion of the cladding material in-pile [9–11]. Two other assumptions assign the accelerated corrosion to the amorphization and the dissolution of the $Zr(Fe,Cr)_2$ precipitates under irradiation [3,12–16].

As shown by Gilbon et al. [17], irradiation in reactor significantly changes the oxidation rate of Zy4 cladding compared to out-of-pile corrosion experiments [17] by affecting several components of the reactor core: the cladding metal, the oxide layer formed on the cladding and the primary coolant. The effects of irradiation of each component on the corrosion rate of the fuel cladding is not currently fully understood. Some progress in this area was recently made on the impact of defects induced by ion irradiation in the oxide on the oxidation rate of Zy4alloy [2,18]. **The present work is devoted to the study of the effects of metal irradiation on the oxidation rate of Zy4.**

1.1. Neutron irradiation effects on the metallurgical state of zy4

Neutron irradiation of cladding in PWR changes the metallurgical state of the Zy4 metal matrix. The following modifications have been observed:

1. rapid increase in the <a> dislocation loop density with irradiation dose [19–21];
2. <c> dislocation loops produced above 5 dpa [22,23] dpa means displacement per atom and the number of dpa describes the nuclear damage level and more specifically the number of times the atoms of the target have moved from their position in the damaged area-;
3. progressive amorphization of intermetallic precipitates (hcp $Zr(Fe,Cr)_2$) usually called Second Phase Precipitate and abbreviated SPP [21,24,25];
4. iron depletion from the SPPs [22,24];
5. iron enrichment of the matrix.

* Corresponding author.
E-mail address: marc.tupin@cea.fr (M. Tupin).
[1] Romain Verlet is now at EDF, EDF R&D, Centre des Renardières, Ecuelles, Moret-sur-Loing Cedex, 77818, France.

https://doi.org/10.1016/j.corsci.2018.02.023
Received 17 November 2017; Received in revised form 31 January 2018; Accepted 16 February 2018
Available online 21 February 2018
0010-938X/

More specifically, < a > dislocation loops located in prismatic planes with Burgers vector b = 1/3⟨11$\bar{2}$0⟩ are observed to form above a very low neutron fluence of around $5{\cdot}10^{23}$ neutrons m^{-2}. The loops density and size increase rapidly with the fluence. The density saturates at around $3{\cdot}10^{22}$ m^{-3} for a relatively low fluence of approximately 10^{24} neutrons m^{-2} which corresponds to 2 cycles in PWR. No significant evolution of the loop size is observed above 10^{24} neutrons m^{-2}. The type of the loops, interstitial or vacancy, depends on the irradiation temperature. Below 300 °C, most of the loops are of the interstitial type [19–21]; the fraction of vacancy loops increases with irradiation temperature. This observation is in agreement with computations from Arévalo et al. using a Monte Carlo method [26]. From a mechanical properties point of view, the increase in < a > dislocation loops, as well as neutron irradiation in general, induce a strong hardening of zirconium alloys. Hardening increases very quickly in-pile and saturates above 10^{24} neutrons.m^{-2} which is a threshold similar to the one observed for the increase in the < a > dislocation loop density. This mechanical hardening decreases very slightly with irradiation temperature between 20 °C and 360 °C [27]. However, above 400 °C, a strong decrease of hardening occurs due to recovery of irradiation defects.

< a > dislocation loops and/or hardening can modify the chemical and mechanical equilibrium at the metal/oxide interface and can subsequently change the corrosion rate of Zy4.

Secondly, progressive amorphization of SPPs is observed above a neutron fluence of 3.10^{25} neutrons m^{-2}.This process starts at the periphery of the SPPs. During the amorphization process, iron is also depleted from the amorphized part of the SPPs and the matrix surrounding the SPP is thus enriched in iron. Finally, < c > -loops, which are vacancy type loops situated in the basal plane, start to appear at a higher damage level (> 5 dpa corresponding to 3.10^{25} neutrons m^{-2}) than < a > dislocation loops. < c > -loops were widely studied in the literature because of their role on the irradiation growth process of the cladding tubes in service [28]. However the target of this work is not focused on the influence of < c > loops on corrosion since they would require extensive ion-irradiation duration in order to be formed in our samples. Our primary focus is thus on the effect of < a > dislocation loops.

In addition, it has been well established that SPPs [29,30] are responsible for the good corrosion resistance of zirconium alloys in high pressure steam and primary water. It is thus interesting to study the role of the amorphization of the SPPs as well as the dissolution of iron in the matrix on the corrosion behavior of Zy4.

The goal of this work is to separate the influence of each metallurgical change induced by irradiation on the corrosion rate. To reach this target, specific ion irradiation parameters were defined using literature data based on ion-irradiation in order to get < a > dislocation loops, complete amorphization (in addition to < a > -loops) and/or iron enrichment of the matrix (in addition to amorphization of the SPPs and < a > -loops).

1.2. Ion irradiation effect on the metallurgical state of the zy4 alloy

As observed by Zu et al. [31], proton irradiation at 350 °C generates < a > dislocation loops without amorphizing SPPs. The loops size and density increase with fluence from the start of the oxidation process. The loop size and density observed with the type of irradiation used in [31] are similar to those observed in PWR. Hardness measurements also evidenced that the hardening induced by proton irradiation at 350 °C is close to the one measured on neutron irradiated cladding. Zu et al. [31] also observed that partial amorphization of SPPs occurs when the irradiation temperature is decreased or when heavier ions are used [31]. Heavy ions also create < a > and < c > loops but the size is lower and the density is higher [32]. Motta et al. [33,34] showed that complete amorphization can be achieved with helium ion irradiation at −196 °C and 0.4 dpa. For heavier ions like Ar or Zr, amorphization is reached at around 1 dpa at room temperature. Finally, it is very difficult to reproduce the iron depletion of the amorphized part of the SPPs by using ion irradiation. However, iron enrichment of the α-Zr matrix can be simulated by implanting iron ions.

In this paper, the experimental approach is first detailed, followed by the characterization of the microstructure of the materials after irradiation. Then the corrosion behavior is studied by weight gain and oxygen diffusion profile. Finally, the discussion is focused on how the corrosion kinetics are impacted by the metallurgical changes induced by irradiation.

Table 1
Chemical composition of the Zy4alloy used in this study (wt%).

Alloying elements	Fe	Cr	Sn	O	H, ppm	Zr
Zy4	0.22	0.11	1.46	0.13	21	Bal.

2. Materials and experiments

2.1. Materials

Sheets of recrystallized Zy4 supplied by AREVA NP were used for this study. The chemical composition of the alloy is given in Table 1. The specimens were cut from a 0.425 mm thick cold-worked sheet which received a final heat treatment of recrystallization at 700 °C for 2 h. The alloy microstructure is characterized by an average grain size of about 10 µm [24]. Final polishing of the samples' surface was performed with diamond paste down to ¼ µm on both sides. The samples are in the form of a coupon with the following dimensions: 15 mm long, 10 mm large and 0.425 mm thick.

2.2. Experimental approach

The experimental approach is similar to that presented in reference [2], however an important difference is that, in the present study, irradiation of the metal is carried out before oxidation in order to study the effect of metal irradiation on corrosion (while in reference [2] irradiation is performed after oxidation in order to study the effect of oxide irradiation on corrosion).

Proton irradiation at 350 °C was performed on two coupons in order to produce only < a > dislocation loops with size and density of the same order than those found in cladding from PWRs. Zirconium ion irradiation of one sample was carried out at room temperature in order to totally amorphize intermetallic precipitates. In this case, < a > loops were also created but the size and density of the loops are theoretically different (of smaller size and higher density) than those generated by protons at high temperature. Finally, iron enrichment in α-Zr matrix was simulated by iron implantation since, as previously mentioned, iron depletion from the SPPs cannot be reproduced with ions. Two fluences of iron ions were chosen to enrich the iron concentration to 0.1 and 0.2 at.% at a depth of 2 µm from the surface.

All experiments and irradiation parameters (ion energy, temperature, fluence) are specified in Table 2.

Figs. 1 and 2 show the distribution of nuclear damage (Φ) simulated by the SRIM software (in displacement per atom (dpa)) in the metal after proton irradiation at 350 °C with a fluence of 10^{18} cm^{-2} and zirconium ion irradiation at room temperature with a fluence of 4.10^{14} cm^{-2} respectively. The dpa values are deduced from the SRIM calculation as described in [2].

Between the surface and the depth of around 1.2 µm in the metal, nuclear damage varies between 0.5 and 1 dpa. The damage increases up to around 5 dpa close to the proton implantation peak.

For zirconium ion irradiation, nuclear damage ranges from 0.2 to 0.9 dpa from the surface up to the maximum which is reached at a depth of 1.2 µm.

Table 2
Irradiation experiments and irradiation parameters.

Ion	Ion energy	Temperature (°C)	Fluence (ions/cm^2)	Flux (ions/cm^2/s)	dpa (at the damage peak)	dose (dpa/s)	Target
H^+	300 keV	**350 °C**	10^{18}	8×10^{13}	4.9	3.9×10^{-4}	**< a > dislocation loops**
Zr^+	6 MeV	**20 °C**	4×10^{14}	2.5×10^{10}	0.9	5.6×10^{-5}	**amorphization** of SPPs + loops
Fe^+	1 MeV	**20 °C**	2.5×10^{15}	4.3×10^{11}	0.6	1.1×10^{-4}	**iron enrichment of the matrix at 0.1 at % +** amorphization of SPPs + loops
Fe^+	1 MeV	**20 °C**	5×10^{15}	4.3×10^{11}	1.3	1.1×10^{-4}	**iron enrichment of the matrix at 0.2 at % +** amorphization of SPPs + loops

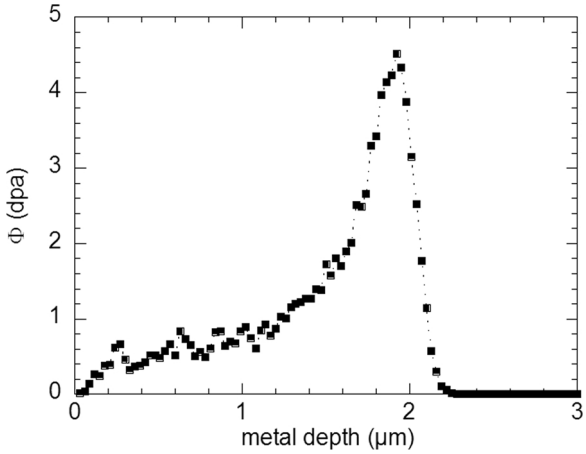

Fig. 1. SRIM simulation of nuclear damage in the metal after 300 keV proton irradiation at a fluence of 10^{18} cm^{-2} (calculations in Full Cascade mode).

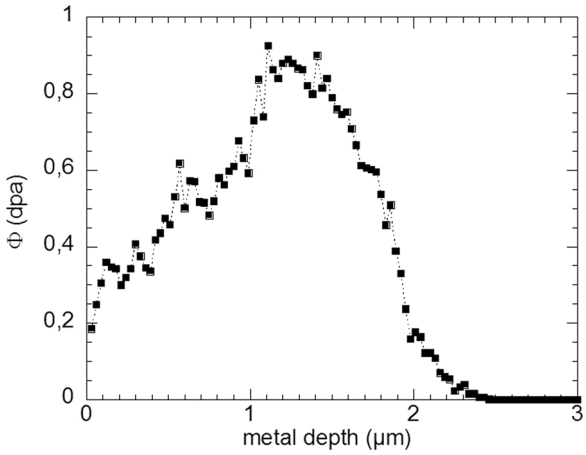

Fig. 2. SRIM simulation of nuclear damage in the metal after 6 MeV Zr ion irradiation at a fluence of 4×10^{14} cm^{-2} (calculations in Full Cascade mode).

Fig. 3 shows the SRIM simulation of the iron distribution in the metal after implantation considering an initial iron concentration in the matrix of 0.2 at.% (see Table 1).

All ion irradiation experiments were performed at the CSNSM JANNUS-Orsay (ARAMIS accelerator) of the University Paris Sud or at the JANNUS-Saclay facilities (with JAPET and EPIMETHEE accelerators).

2.3. TEM characterization after irradiation

Characterization of the irradiation damage was performed with a 30 G2 Tecnai Transmission Electron Microscope (TEM) from FEI operating at 300 kV. Thin foils were first machined by mechanical polishing and finally polished with a soft ion beam of Argon using a PIPS (Precision Ion Polishing System), in order to observe the nuclear damage close to the surface after irradiation. For samples irradiated with protons, cross-sectional thin foils were extracted with the Focused Ion Beam technique (cutting out and thinning with a Ga^+ ion beam) to characterize the microstructure of the sample parts close to the nuclear damage maximum (at a depth of around 2 μm beneath the surface, as seen in Fig. 1).

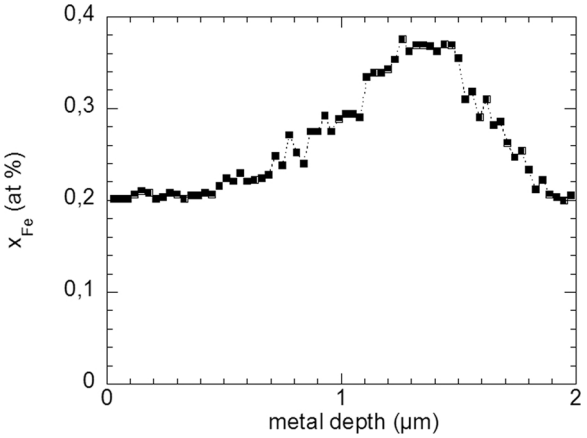

Fig. 3. SRIM simulation of iron implantation in the metal after 1 MeV iron ion irradiation at a fluence of 5×10^{15} cm^{-2} (calculations in Full Cascade mode).

2.4. Corrosion tests

Irradiated samples as well as reference unirradiated samples were corroded in static autoclaves, in light primary water environment ($H_2{}^{16}O$) at 360 °C and 18.7 MPa of pressure with 2 wt.ppm of lithium and 1000 wt.ppm of boron from lithium hydroxide and boric acid added to the water. The oxidation kinetics were followed by measuring the weight of the samples every 2–4 weeks. Both unirradiated and irradiated samples were weighted with a SARTORIUS MC 210 P scale. The precision of the scale is 2.10^{-5} g.

2.5. Isotopic exposure and SIMS analyses

The oxidation rate is limited by oxygen diffusion through the oxide layer. Therefore, isotopic markers of oxygen such as ^{18}O were used in this study to understand the diffusion process. Corroded specimens up to 1.5 μm oxide thickness were oxidized in a final corrosion step during 24 h in a mixture enriched with 20% of $H_2{}^{18}O$ (in volume). ^{18}O diffusion profiles in the oxide were then analyzed by Secondary Ion Mass Spectrometry using a CAMECA® IMS 7F at GeMaC CNRS laboratory of the University of Versailles Saint-Quentin-en-Yvelines. A primary 10 keV ion beam and a current of 40 nA of Cs^+ were used to abrade the material. The sputtering area was a square of 150 × 150 μm^2. Negative secondary ions were collected from an analyzed surface of 33 μm in diameter. The data analysis method has been described in details in reference [2].

Table 3
Samples, analysis methods used, oxide thicknesses for SIMS and TEM analyses and oxide thicknesses at the end of the oxidation test.

Sample ion/fluence	number of coupons	SIMS analysis	oxide thickness for SIMS analysis (μm)	TEM analysis	oxide thickness for TEM analysis (μm)	total exposure time (days)	final oxide thickness at the end of the oxidation test (μm)
unirradiated reference	1	yes	~1.4	yes	~1.1	190	3.35 +/− 0.15
$H^+/10^{18}\,cm^{-2}$	2	yes	~1.5	yes	~1.3	160	4.2 +/− 0.2
$Zr^+/4 \times 10^{14}\,cm^{-2}$	1	yes	~1.5	–	–	190	3.55 +/− 0.15
$Fe^+/2.5 \times 10^{15}\,cm^{-2}$	1	yes	~1.4	–	–	190	3.45 +/− 0.15
$Fe^+/5 \times 10^{15}\,cm^{-2}$	1	yes	~1.4	–	–	190	3.2 +/− 0.15

2.6. TEM characterization after oxidation

Similarly to the TEM characterization of irradiated samples, cross-sectional thin foils of oxidized samples were extracted by a Focused Ion Beam to characterize the oxide microstructure of the samples irradiated with protons.

Table 3 summarizes the analysis methods and the oxide thicknesses at which SIMS and TEM analyses were performed. The total exposure time and the oxide thicknesses reached at the end of the corrosion test are also indicated.

3. Experimental results

First of all, metal characterizations with TEM were performed after irradiation in order to observe the microstructural evolution of the metal.

3.1. Microstructure of the metal before oxidation

3.1.1. Proton irradiation

Figs. 4a et b present respectively the metallurgical states of the unirradiated sample and the matrix irradiated with protons (see Table 2 for irradiation parameters). While the reference matrix has very few dislocations, a high density of irradiation defects is observed in Fig. 4b. According to literature data [27,31], these defects are likely to be dislocation loops. No quantitative measurement of their density and size has been done during this work. However, since the nuclear damage level is well below 5 dpa, the observed loops are likely < a > dislocation loops and their density is likely to be around $10^{22}\,cm^{-2}$ according to the work of Zu et al. [31].

It is important to note that the electron diffraction patterns of Fig. 4b show, as expected, that the SPPs seem to remain mainly crystalline after irradiation. Indeed in the case of amorphized SPP, the diffraction pattern would present diffuse rings as observed for the ion-irradiation conditions used in the next paragraph. TEM characterizations close to the surface were also carried out and led to similar conclusions.

In summary, irradiation with 300 keV protons at a nuclear damage below 5 dpa produces, as expected, a high density of dislocation loops (likely < a > type loops) without amorphizing the SPPs.

3.1.2. Zr and Fe ion irradiation

Figs. 5 and 6 present respectively the matrix irradiated with Zr and Fe ions (see Table 1 for irradiation parameters). The thin foils were extracted from the sample surface (where the damage level is the lowest, around 0.2 dpa) by ionic polishing.

While the reference matrix (see Fig. 4a) has crystalline SPPs, these SPPs after irradiation with Zr ions become amorphous as shown by the diffuse ring observed on the corresponding electron diffraction pattern as well as the absence of diffraction contrast inside the SPP (Fig. 5). Irradiation with Fe ions also induces amorphization of the SPPs because there is no diffraction contrast inside the SPP as seen in Fig. 6. Contrarily to amorphized SPPs, TEM image of crystalline SPP presented on Fig. 4a exhibit a high contrast inside the SPP.

It also seems that there are very few dislocation loops in the matrix irradiated with zirconium and iron ions compared to the matrix irradiated with protons despite the fact the crystalline orientation of the thin foil was not optimized to reveal these defects.

Finally, it is important to note that, for both samples irradiated with Zr and Fe ions, all of the analyzed $Zr(Fe,Cr)_2$ precipitates are amorphized even at the sample surface where the damage level is the smallest.

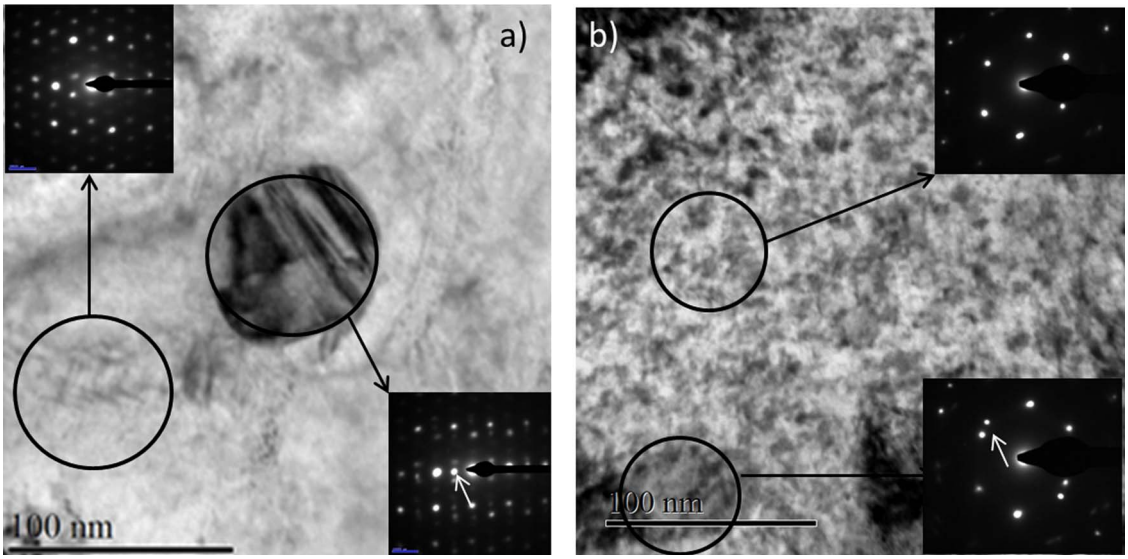

Fig. 4. a) Bright field TEM image and electron diffraction patterns of the unirradiated matrix and a crystalline precipitate $Zr(Fe,Cr)_2$ (the white arrow indicates a dot corresponding to the diffraction of the crystalline precipitate). b) Bright field TEM image and electron diffraction patterns of the irradiated matrix with 300 keV protons at a fluence of $10^{18}\,cm^{-2}$ and a crystalline precipitate $Zr(Fe,Cr)_2$ (the white arrow indicates a dot corresponding to the diffraction of the crystalline precipitate).

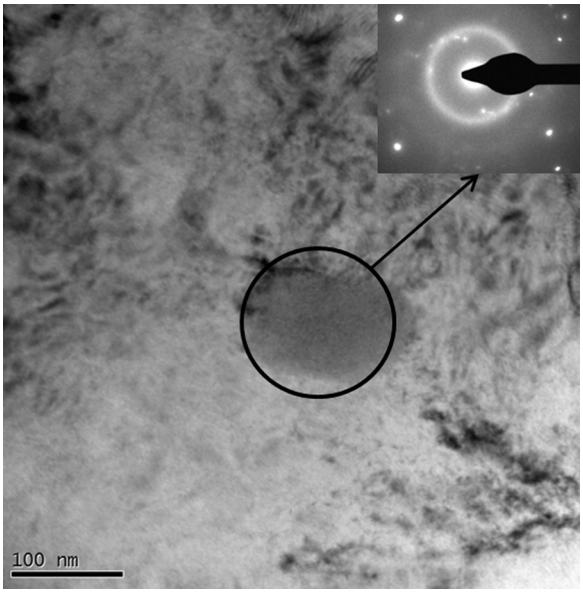

Fig. 5. Bright field TEM image and electron diffraction patterns of the matrix irradiated with Zr ions at a fluence of $4 \times 10^{14}\,cm^{-2}$ and an amorphous precipitate $Zr(Fe,Cr)_2$ (the diffuse ring is characteristic of the amorphous state of the SPP).

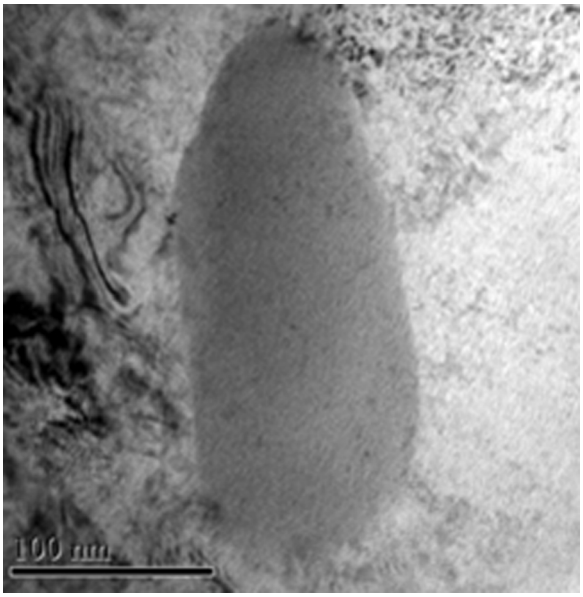

Fig. 6. Bright field TEM image of the matrix irradiated with Fe ions at a fluence of 2.5×10^{15} and $5 \times 10^{15}\,cm^{-2}$ and an amorphous precipitate $Zr(Fe,Cr)_2$ (no contrast inside the SPP).

3.2. Irradiation effect on the oxidation rate

3.2.1. Proton irradiation

Oxidation kinetics after irradiation with protons are compared to those obtained for the unirradiated material in Fig. 7b. Fig. 7a shows the nuclear damage level of the matrix affected by the advanced oxidation front. Metal irradiation with protons induces a significant increase in the oxidation rate during the first days of corrosion. During the pre-transition stage, the oxidation rate after irradiation is approximately around 1.5 times higher than that of the unirradiated material. After the kinetics transition, which occurs at an oxide thickness of about 1.8 μm, the oxidation rate of irradiated metal remains higher compared to the reference material, however the oxidation rate no longer follows the variations of the nuclear damage level. The oxidation rate ratios between the irradiated material and the unirradiated one are indeed similar at the beginning of corrosion and at 3 μm which corresponds to the highest damaged area (represented by a dotted line).

As explained previously, some of the specimens corroded up to around 1.5 μm oxide thickness (black dotted circles in Fig. 7b indicating the oxide thicknesses at which the samples were exposed in ^{18}O enriched environment) were oxidized during a final step for 24 h in a mixture enriched with 20% of $H_2{}^{18}O$ (in volume). ^{18}O diffusion profiles in the oxide were then analyzed by Secondary Ion Mass Spectrometry as shown in Fig. 8a. The ^{18}O intensity across the oxide layer formed on the proton irradiated matrix is higher than that measured on the unirradiated sample at all measured depths.

The average oxygen diffusion flux in the irradiated material exposed 24 h to the solution enriched in ^{18}O can be compared to the average diffusion flux through the oxide of the unirradiated material using the following formula (Eq. (1)) (see Ref. [2]):

$$\frac{\left\langle J^{\varphi}_{^{18}O} \right\rangle}{\left\langle J^{NI}_{^{18}O} \right\rangle} = \frac{\int_0^{e_{ox}} I^{\varphi}_{^{18}O}\,dx}{\int_0^{e_{ox}} I^{NI}_{^{18}O}\,dx} \quad (1)$$

where $I^{\varphi}_{^{18}O}$ and $I^{NI}_{^{18}O}$ are, respectively, the ^{18}O SIMS profile intensities of the irradiated (ϕ) and the non-irradiated materials (NI). $\left\langle J^{\varphi}_{^{18}O} \right\rangle$ and $\left\langle J^{NI}_{^{18}O} \right\rangle$ are, respectively, the average diffusion fluxes of ^{18}O in the oxide irradiated at the fluence ϕ or not irradiated (NI) during 24 h. e_{ox} is the oxide thickness.

The ratio of the average diffusion fluxes during the isotopic exposure time is then deduced from the ratio of the ^{18}O integrated signals. Basically, this ratio is around 1.5. This value is close to the ratio of the oxidation rates measured on the kinetics curves indicated on Fig. 8b which is around 1.45 for 1.5 μm oxide thickness. It should be noted that the added hydrogen content from the proton irradiation is 7 wt.ppm which corresponds to the level of hydrogen initially present in the sample. Thus the effect of hydrogen on the corrosion rate of the proton-irradiated experiments studied here is likely negligible.

3.2.2. Zr and Fe ion irradiation

Oxidation kinetics after irradiation with Zr and Fe ions are respectively compared to the ones of the unirradiated material in Figs. 9a 10b . Figs. 9a 10a show the nuclear damage level and the iron concentration enrichment of the matrix affected by the advanced oxidation front respectively.

It is clear according to these figures that neither Zr ion irradiation nor Fe ion irradiation of the Zy4 matrix have a significant effect on the corrosion behavior of the material. This implies that neither amorphization of the SPPs nor iron enrichment plays a major role on the oxidation resistance. These conclusions are confirmed by ^{18}O SIMS profiles shown on Fig. 11a and b for Zr ion irradiation and Fe ion irradiation.

^{18}O diffusion profiles obtained on irradiated samples are nearly superimposed on the SIMS profile of oxygen recorded for the unirradiated material. However the oxygen profile of the Zr ion irradiated specimen is slightly higher than the reference oxygen profile, especially close to the surface. This observation is consistent with the slight increase in the oxidation rate observed on Fig. 9b at 1.5 μm oxide thickness corresponding to the oxidation of the most damaged part of the metal.

3.3. Oxide microstructure formed on proton irradiated sample

The oxide microstructure formed on the unirradiated specimen and the proton irradiated sample are characterized with TEM as shown in Figs. 12 and 13, respectively. The samples are corroded during 30 days for the reference specimen and 14 days for the irradiated material. The

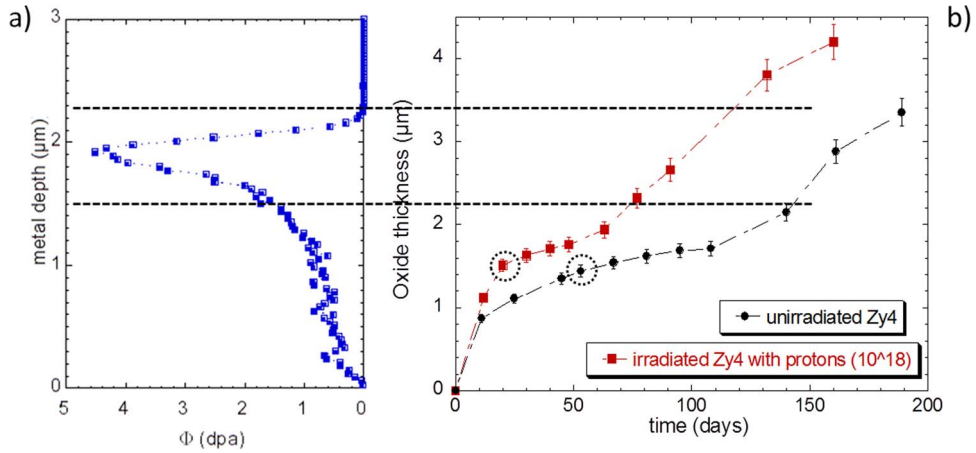

Fig. 7. a) Damage profile in the matrix of Zy4 sample irradiated with 300 keV protons at a fluence of 10^{18} cm^{-2} and 350 °C. b) Oxidation kinetics of unirradiated sample and sample irradiated with 300 keV protons at a fluence of 10^{18} cm^{-2} and 350 °C. Black dotted circles indicate the oxide thicknesses at which the samples were exposed in ^{18}O enriched environment.

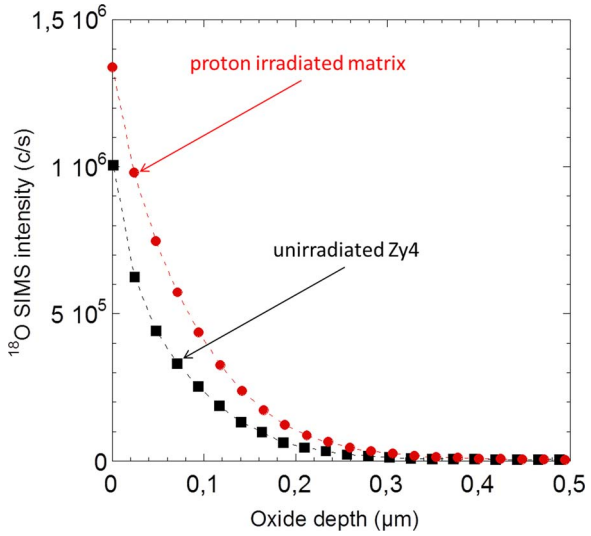

Fig. 8. a) ^{18}O SIMS profiles in the oxide layer after 24 h isotopic exposure for unirradiated (dark squares) and Zr ion irradiated samples (red circles) b) fitted power laws for proton irradiated (red curve) and unirradiated (black curve) materials and oxidation rate ratio at 1.4-1.5 µm oxide thicknesses in the red frame. Black dotted circles indicate the oxide thicknesses at which the samples were exposed in ^{18}O enriched environment. (For interpretation of the references to colour in this figure legend, the reader is referred to the web version of this article.)

oxide thicknesses measured from the TEM micrographs vary in the range of 1.1–1.2 µm for the unirradiated sample and of 1.3–1.6 µm for the irradiated Zy4. These are consistent with the oxide thicknesses deduced from the weight gains and confirms the fact that the oxidation rate is significantly higher for the proton irradiated sample compared to that of the unirradiated sample. The most significant microstructural difference observed is the presence of many cracks in the oxide formed on the proton irradiated specimen (Fig. 13) while the oxide layer formed on the reference sample is more homogeneous without micrometric cracks (Fig. 12).

At a higher magnification focused on the outer part of the oxide, the TEM images of Figs. 14 and 15 reveal an external microstructure different between the irradiated sample and the reference one.

The sublayer beneath the surface of the irradiated sample is very irregular with a high density of nano-sized pores or short-circuits as illustrated in Fig. 15 until a depth of 100 nm in the oxide layer. These could play a significant role on the oxidation rate. This sublayer is not observed on the reference material but it does not mean that there is no pore in the oxide [35]

3.4. Discussion on irradiation effects

3.4.1. Effect of the SPPs amorphization on the oxidation kinetics

All the SPPs after room temperature irradiation of the metal with heavy ions (Fe and Zr) are fully amorphized in the damaged areas observed (Figs. 5 and 6). Despite this metallurgical change, the corrosion behavior of the Zy4 alloy does not seem to be affected. This implies that the crystallinity of the SPPs is not solely responsible for the corrosion

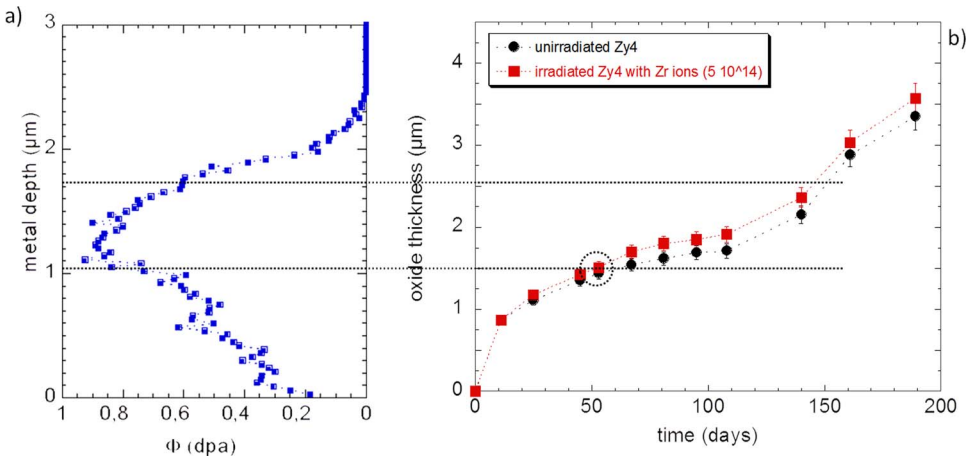

Fig. 9. a) Damage profile in the matrix of Zy4 sample irradiated with 6 MeV Zr ions at a fluence of 5×10^{14}cm^{-2} and at room temperature. b) Oxidation kinetics of unirradiated sample (black dots) and sample irradiated with 6 MeV Zr ions at a fluence of 5×10^{14}cm^{-2} and at room temperature (red squares). Black dotted circle indicates the oxide thickness at which the samples were exposed in ^{18}O enriched environment. (For interpretation of the references to colour in this figure legend, the reader is referred to the web version of this article.)

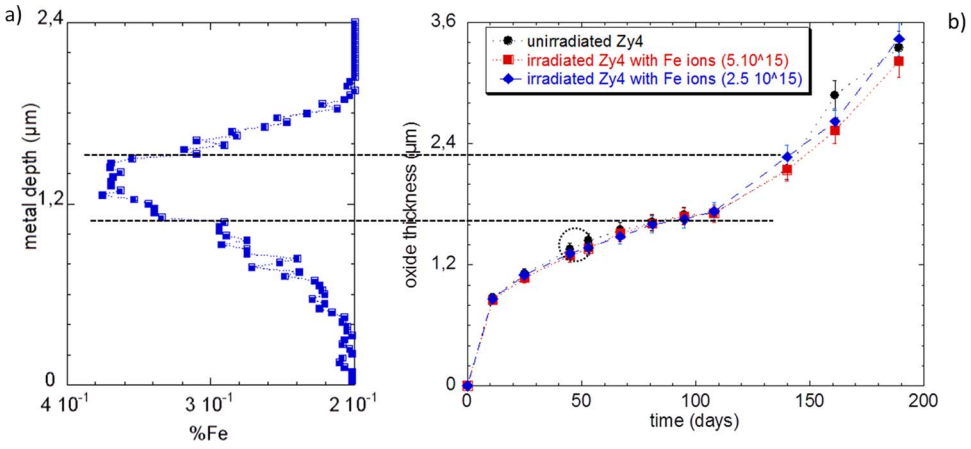

Fig. 10. a) Iron concentration in the matrix of Zy4 sample implanted with 1 MeV Fe ions at a fluence of 5×10^{15} cm^{-2} and at room temperature. b) Oxidation kinetics of unirradiated sample (black dots) and sample irradiated with 1 MeV Fe ions at a fluence of 2.5×10^{15}cm^{-2} (blue diamonds) and 5×10^{15}cm^{-2} (red squares) and at room temperature. Black dotted circle indicates the oxide thickness at which the samples were exposed in ^{18}O enriched environment. (For interpretation of the references to colour in this figure legend, the reader is referred to the web version of this article.)

resistance of Zy4 and their amorphization does not modify significantly the oxidation rate of the material.

However, the amorphous state of the SPPs has not been verified after the corrosion test and we suppose that the precipitates remain in this state all along the corrosion process. The fact that there is no effect since the first step of corrosion supports this hypothesis. Pêcheur [34] had also showed that amorphization of the precipitates lasted more than 3 days after a corrosion test in steam at 415 °C and 10 MPa of irradiated Zy4 matrix with helium ions at a similar damage level (~1 dpa).

Finally, in spite of the lack of characterization after the corrosion test, it is very likely that the amorphization process of the $Zr(Fe,Cr)_2$ precipitates is not responsible for the strong acceleration of the kinetics observed at high burnup in reactor.

3.4.2. *Effect of iron enrichment of the matrix*

For both iron concentrations implanted in the α-Zr matrix, no effect on the oxidation rate has been observed. Iron enrichment is localized, according to the SRIM simulation, between 1 and 1.5 µm beneath the surface. However the actual distribution of iron was not characterized in this study. It is also unclear whether iron remains effectively in solid solution in the matrix or whether it precipitates during the thermal annealing in autoclave.

Finally, to definitely conclude about the impact of iron dissolution in the matrix, it would be useful to characterize the evolution of the iron distribution in the matrix during the corrosion process.

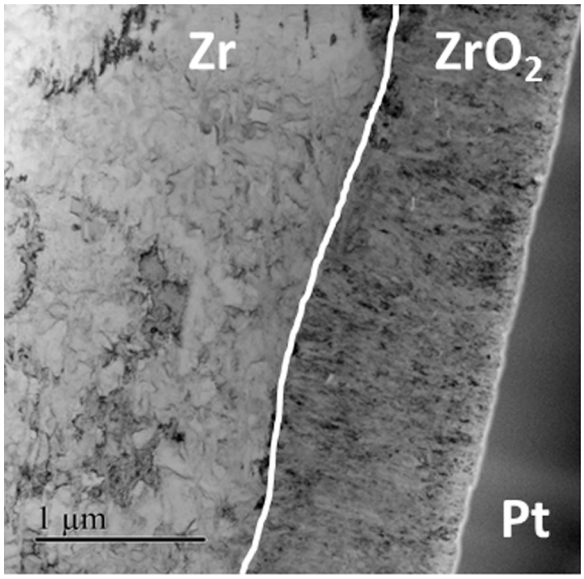

Fig. 12. Cross-section TEM image of the oxide layer formed on the proton irradiated metal during 14 days exposure time.

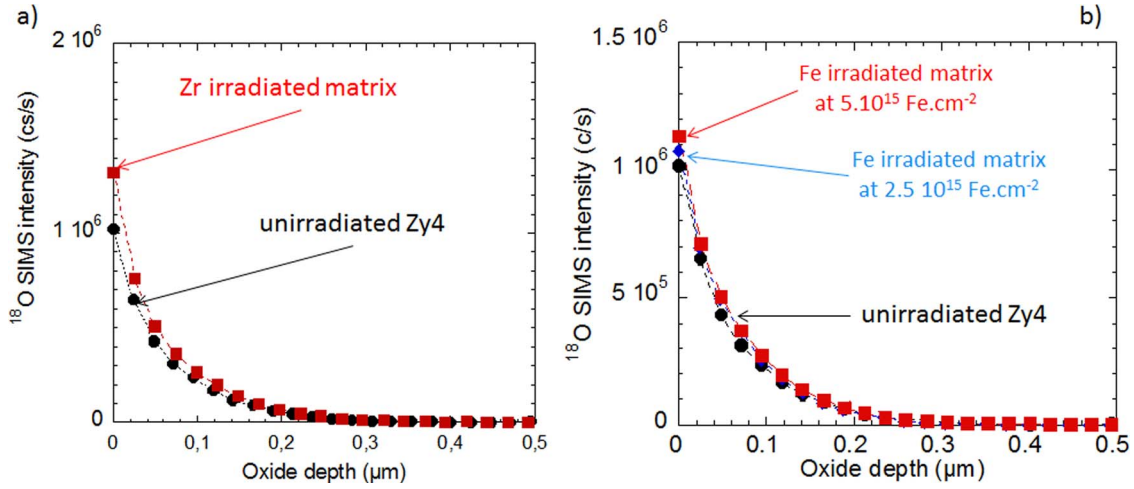

Fig. 11. a) ^{18}O SIMS profiles in the oxide layer after 24 h isotopic exposure for non-irradiated material (dark circles) and Zr ion irradiated samples (red squares). b) ^{18}O SIMS profiles in the oxide layer after 24 h isotopic exposure for non-irradiated material (dark squares) and **Fe** ion irradiated samples at a fluence of 2.5×10^{15}cm^{-2} (blue diamonds) and of 5×10^{15} cm^{-2}(red circles). (For interpretation of the references to colour in this figure legend, the reader is referred to the web version of this article.)

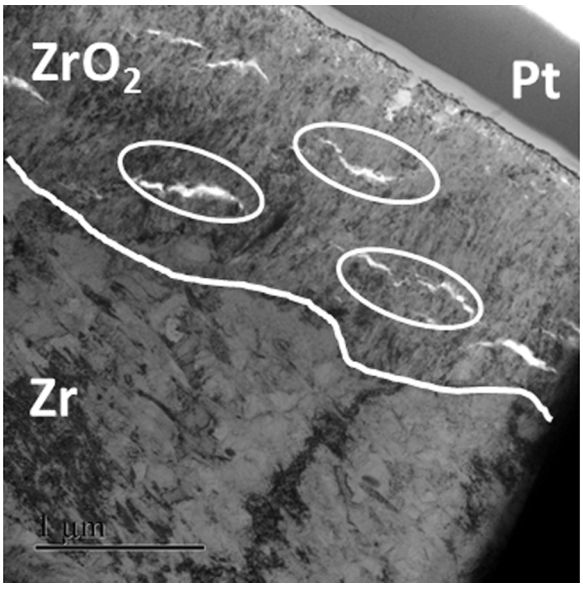

Fig. 13. Cross-section TEM image of the oxide layer formed on the unirradiated sample during 30 days exposure time.

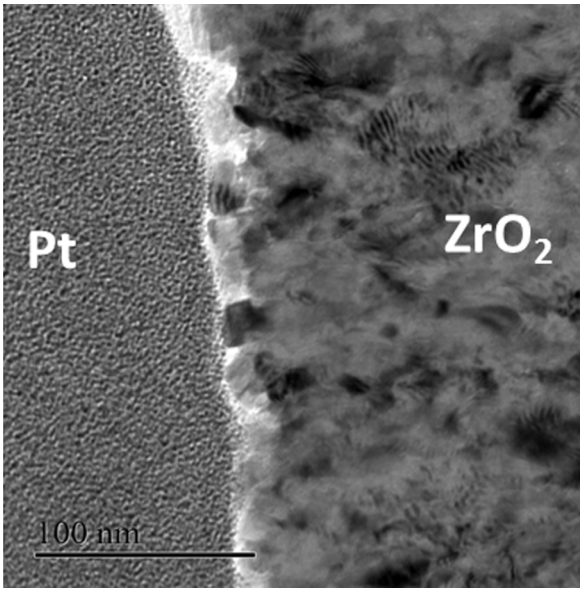

Fig. 14. TEM image of the outer part of the oxide formed on the unirradiated sample during 30 days exposure time.

3.4.3. Potential effect of < a > dislocation loops on the oxidation rate

Proton irradiation of the metal created a high density of < a > dislocation loops by nuclear damage as shown in Fig. 4b. It induced a significant increase in the oxidation rate from the beginning of the corrosion test up to the post-transition stage (Fig. 7b). It is also well known that neutron or ion irradiation induce a strong hardening of the matrix in the damaged area for irradiation temperatures below 400 °C [16,27,36]. High density of < a > dislocation loops and irradiation hardening are coupled phenomena that can be responsible for the acceleration of the oxidation kinetics.

However, irradiations with Zr or Fe ions theoretically produce also nuclear damage. As a result < a > dislocation loops formation as well as irradiation hardening could both occur (even if these loops are not clearly evidenced on TEM characterizations). However, samples irradiated with Fe/Zr ions do not exhibit any significant acceleration of the corrosion kinetics. Thus how can this difference of corrosion behavior after irradiation and formation of < a > dislocation loops be explained?

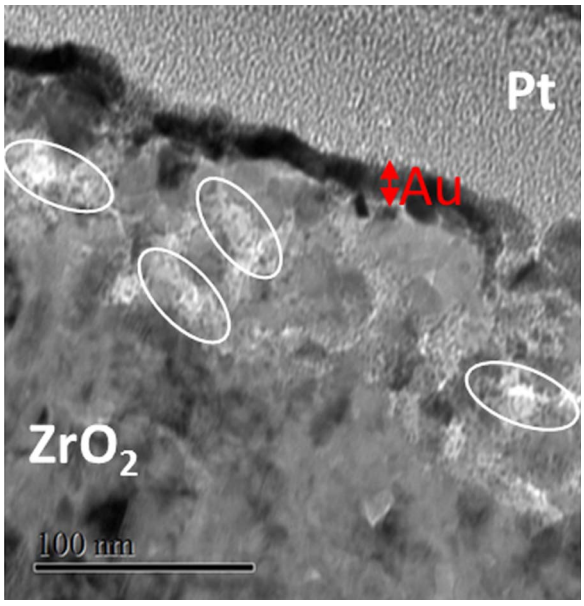

Fig. 15. Cross-section TEM image of the oxide layer formed on the unirradiated sample during 30 days exposure time.

The biggest difference between the proton and the heavy ion experiments is the irradiation temperature, 350 °C for the protons and room temperature for heavier ions. According to Idrees et al. [37], the average size of < a > dislocation loops increases with irradiation dose and with temperature (temperature range investigated from 300 to 500 °C) while the loop density decreases. It is thus likely that proton irradiation at 350 °C generates greater loop size with a lower density than those obtained after heavy ion irradiation at room temperature.

Secondly, the type of < a > dislocation loops, vacancy or interstitial, can potentially vary depending on the ion used in the irradiation experiments. In addition, the proportion of vacancy to interstitial loops increases especially with irradiation temperature [19,21]. While, at low irradiation temperature (below 300 °C), the majority of loops present in the material are of the interstitial type, a ratio of around 50% of vacancy loops is reached after neutron irradiation at 350 °C. Consequently, the difference of impact on kinetics could be due to the difference of distribution and/or loop type between proton and heavy ion irradiation experiments.

However, although the point defects cannot be observed with the conventional TEM analyses, we cannot dismiss the possibility that this difference in corrosion kinetics between proton irradiated material and heavy ion irradiated material results in a difference of point irradiation defect concentrations between experiments.

Thus, we can ask what impact can large < a > dislocation loops have on the oxidation rate.

Three hypotheses can be advanced, the impact on the oxidation rate could be due to a chemical effect, to the change of mechanical properties of the metal or to the crystal state of the oxide.

The large vacancy < a > dislocation loops can induce a modification of the equilibrium of the oxidation reaction at the metal/oxide interface. It is indeed possible that zirconium chemical potential depends on size and density of vacancy loops in the metal. The change of the equilibrium could increase the concentration of oxygen vacancy at the metal/oxide interface. Oxidation rate being controlled by oxygen vacancy diffusion [29] would thus be enhanced by the increase in oxygen vacancy concentration. However, this effect on the oxidation kinetics is observed only if the volume fraction of < a > dislocation loops reaches a critical value. This threshold would likely have not been reached after irradiation with heavy ions.

Secondly, irradiation hardening of the metal can also impact the

corrosion kinetics. As already shown by calculations in the literature, relaxation of compressive stresses in the oxide scale can be due to the development of an interface roughness due to by plastic deformation of the metal [38–41]. Consequently, the increase in hardness of the matrix after irradiation can result in an increase in compressive stresses in the oxide which could be released in this case by generating some cracks in the oxide layer. However, cracks as well as compressive stresses usually tend to reduce the oxygen diffusion flux in the oxide [40,42–44]. So in both cases the oxidation rate should be theoretically lower after irradiation. However, the cracks may generate a porous network for the primary medium which could thus be closer to the metal/oxide interface which would in turn lead to an increase in the oxidation rate. This interpretation is not really supported by the slight difference of the ^{18}O penetration depth between unirradiated and proton irradiated material.

Finally, nucleation of the oxide can also be modified by the dislocation loops present in the matrix. Basically, oxide texture, tetragonal phase volume fraction or misorientation angles of grain boundaries are susceptible to change after metal irradiation which could also result in a modification of the oxidation rate. Advanced characterizations are needed in order to clarify the effect observed [45,46].

From an industrial point of view, the threshold in volume fraction of < a > dislocation loop is probably reached after 1 cycle in reactor because the nuclear damage level is around 2 dpa. This study has shown an increase in the oxidation rate of a matrix irradiated up to 1 dpa with protons. The acceleration factor is in this case between 1.5 and 2. It would be useful in the future to quantify the size and density of the < a > dislocation loops produced by proton irradiation and to compare them with those obtained on cladding in reactor. The acceleration factor due to the loops in reactor could then be estimated.

4. Conclusions

Irradiation effects of the Zy4 metal on the oxidation kinetics as well as on the oxygen diffusion through the oxide have been investigated using different ions producing specific metallurgical states in order to simulate the evolution of the matrix during the lifetime of the fuel rod in PWR. This work has shown that:

1. Proton irradiation at a temperature close to in-core temperature (~350 °C) produces dislocation-loops without modifying the crystalline state of the SPPs. The oxidation rate of the damaged matrix is in this case significantly higher compared with that measured on the unirradiated material.
2. Zr ion irradiation at room temperature induces mainly an amorphization of the SPPs. The modification of the crystalline state of the precipitates does not induce a significant change of the oxidation rate of Zy4.
3. Iron implantation in the matrix does not seem to play a strong role on the corrosion rate. This conclusion however needs additional results to be strengthened.

In the end, three tracks of interpretation of proton irradiation effects have been discussed (chemical effect, mechanical impact and an irradiation effect on the crystal state of the oxide). To validate one of these interpretations, loop size, loop density, irradiation hardening as well as the crystal state of the oxide have to be investigated in more details.

Acknowledgments

EDF and AREVA are acknowledged for their financial support. The writers would like to thank all who have contributed to this study and in particular the staff of JANNUS-Orsay and Jannus-Saclay Facilities.

References

[1] G.L. Garner, B.A. Hilton, E. Mader, Performance of alloy M5™ cladding and structure, LWR Fuel Performance Meeting/Top Fuel, San Francisco, 30th septembre-3th October, 2007.
[2] R. Verlet, M. Tupin, G. Baldacchino, K. Wolski, S. Miro, D. Gosset, K. Colas, M. Jublot, F. Jomard, Corros. Sci. 98 (2015) 327–338.
[3] P. Bossis, B. Verhaeghe, S. Doriot, D. Gilbon, V. Chabretou, J.-P. Dalmais, A. Miquet, In PWR comprehensive study of high burn-up corrosion and growth behavior of M5 and recrystallized low-tin zircaloy-4, Zirconium in the Nuclear Industry, 15th International Symposium, ASTM STP 1505, 2008, pp. 430–456 paper ID JAI101314 available online at www.astm.org.
[4] V. Bouineau, A. Ambard, G. Bénier, D. Pêcheur, J. Godlewski, L. Fayette, T. Duverneix, A new model to predict the oxidation kinectics of zirconium alloys in a Pressurized Water Reactor, Zirconium in the Nuclear Industry, 15th International Symposium, ASTM STP 1505, 2008, pp. 405–429 paper ID JAI10131 available online at www.astm.org.
[5] M. Blat, D. Noel, Detrimental role of hydrogen on the corrosion rate of zirconium alloys, Zirconium in the Nuclear Industry, 11th International Symposium, ASTM STP 1295, 1996, pp. 319–337.
[6] M. Blat, L. Legras, D. Noel, H. Amanrich, Contribution to a better understanding of the detrimental role of hydrogen on the corrosion rate of Zircaloy-4 cladding materials, Zirconium in the Nuclear Industry, 12th International Symposium, ASTM STP 1354, 2000, pp. 563–591.
[7] T. Kido, A Study on Enhanced Uniform Corrosion of Zircaloy-4 Cladding During High Burnup Operation in PWR's, 6th International Symposium on Environmental Degradation of Materials in Nuclear Power Systems, Hardcover, 1993, pp. 449–454.
[8] M. Tupin, C. Bisor, P. Bossis, J. Chêne, J.L. Bechade, F. Jomard, Corros. Sci. 98 (2015) 478–493.
[9] P. Bossis, D. Pêcheur, K. Hanifi, J. Thomazet, M. Blat, Comparison of the high burn-up corrosion on M5 and low tin Zircaloy-4, Zirconium in the Nuclear Industry, 14th International Symposium, ASTM STP 1467, 2005, pp. 494–525 paper ID JAI12404 available online at www.astm.org.
[10] A.M. Garde, A.R. Pati, M.A. Krammen, G.P. Smith, R.K. Endter, Corrosion behavior of zircaloy-4 cladding with varying tin content in high-temperature pressurized water reactors, Zirconium in the Nuclear Industry, 10th International Symposium, ASTM STP 1245, 1994, pp. 760–778.
[11] F. Garzarolli, Y. Broy, R.A. Busch, Comparison of the long-time corrosion behavior of certain Zr alloys in PWR, BWR, and laboratory tests, Zirconium in the Nuclear Industry, 11th International Symposium, ASTM STP 1295, 1996, pp. 12–32.
[12] X. Iltis, F. Lefebvre, C. Lemaignan, Microstructure evolutions and iron redistribution in zircaloy oxide layers: comparative effects of neutron irradiation flux and irradiation damages, Zirconium in the Nuclear Industry, 11th International Symposium, ASTM STP 1295, 1996, pp. 242–264.
[13] X. Iltis, F. Lefebvre, C. Lemaignan, J. Nucl. Mater. 224 (1995) 121–130.
[14] P. Barberis, E. Ahlberg, N. Simic, D. Charquet, C. Lemaignan, G. Wikmark, M. Dahlbäck, M. Limbäck, P. Tägtström, B. Lehtinen, Role of the second-phase particles in zirconium binary alloys, Zirconium in the Nuclear Industry, 13th International Symposium, ASTM STP 1423, 2002, pp. 33–58.
[15] H.J. Jin, T.K. Kim, Annals. Nucl. Energy 75 (2015) 309–315.
[16] P. Dayal, D. Bhattacharyya, W.M. Mook, E.G. Fu, Y.-Q. Wang, D.G. Carr, O. Anderoglu, N.A. Mara, A. Misra, R.P. Harrison, L. Edwards, J. Nucl. Mater. 438 (2013) 108–115.
[17] D. Gilbon, Les matériaux de gaines et d'assemblage Les combustibles Nucléaires, monographie de la DEN, Edition du Moniteur, (2008), p. 38 (Paris).
[18] J. Tupin, D. Hamann, P. Cuisinier, M. Bossis, A. Blat, A. Miquet, D. Kaczorowski, Understanding of corrosion mechanisms of zirconium alloys after irradiation: effect of ion irradiation of the oxide layers on the corrosion rate, Zirconium in the Nuclear Industry, 17th international symposium, ASTM STP 1543, 2014, pp. 438–478.
[19] D.O. Northwood, Atomic Energy Rev. 15 (1977) 547–610.
[20] D.O. Northwood, R.W. Gilbert, L.E. Bahlen, P.M. Kelly, R.G. Blake, P.K. Madden, D. Faulkner, W. Bell, R. B.Adamson, J. Nucl. Mater. 79 (1979) 379–394.
[21] M. Griffiths, J. Nucl. Mater. 159 (1988) 190–218.
[22] M. Griffiths, R.W. Gilbert, V. Fidleris, R.P. Tucker, R.B. Adamson, J. Nucl. Mater. 150 (1987) 159–168.
[23] M. Griffiths, J.F. Mecke, J.E. Winegar, Evolution of microstructure in zirconium alloys during irradiation, Zirconium in the Nuclear Industry, 11th International Symposium; ASTM STP 1295, 1993, pp. 580–602.
[24] A. Gilbon, S. Doriot, J.P. Mardon, Irradiation creep and growth behavior, and microstructural evolution of advanced Zr-base alloys, Zirconium in the Nuclear Industry, 12th international symposium, ASTM STP 1354, 2000, pp. 51–73.
[25] A.T. Motta, F. Lefebvre, C. Lemaignan, Amorphization of precipitates in Zircaloy under neutron and charged-particles irradiation, Zirconium in the Nuclear Industry, 9th international symposium, ASTM STP 1132, 1991, pp. 718–739.
[26] C. Arevalo, M.J. Caturla, J.M. Perlado, J. Nucl. Mater. 362 (2007) 293–299.
[27] F. Onimus, J.L. Bechade, Radiation Effects in Zirconium Alloys, Comprehensive Nuclear Materials, Elsevier, Oxford, 2012.
[28] V. Fidleris, J. Nucl. Mater. 159 (1988) 22–42.
[29] Y. Dali, M. Tupin, P. Bossis, M. Pijolat, J. Nucl. Mater. 426 (2012) 148–159.
[30] E. Barberis, N. Ahlberg, D. Simic, C. Charquet, G. Lemaignan, M. Dahlbäck, M. Limbäck, P. Tägtström, B. Lehtinen, Role of the second-phase particles in zirconium binary alloys, Zirconium in the Nuclear Industry, 13th International Symposium, ASTM STP 1423, 2002, pp. 33–58.
[31] X.T. Zu, K. Sun, M. Atzmon, L.M. Wang, L.P. You, F.R. Wan, J.T. Busby, G.S. Was, R.B. Adamson, Philos. Mag. 85 (2005) 649–659.
[32] B. Doriot, D. Bechade, D. Menut, J.P. Mardon, J.M. Cloue, A. Miquet, L. Legras, Microstructural evolution of M5™ alloy irradiated in PWRs up to high fluences –comparison with other Zr-based alloys, Zirconium in the Nuclear Industry, 17th International Symposium, ASTM STP 1543, 2015, pp. 759–799.

[33] A.T. Motta, F. Lefebvre, C. Lemaignan, Amorphization of precipitates in Zircaloy under neutron and charged-particles irradiation, Zirconium in the Nuclear Industry, 9th international symposium, ASTM STP 1132, 1991, pp. 718–739.
[34] D. Pêcheur, Evolution des précipités à base zirconium lors de l'oxydation et de l'irradiation d'alliages de Zr, PhD Thesis de l', Institut National Polytechnique de Grenoble, 1993.
[35] N. Ni, S. Lozano-Perez, M.L. Jenkins, C. English, G.D.W. Smith, J.M. Sykes, C.R.M. Governor, Scripta Mater. 62 (2010) 564–567.
[36] Chunguang Yan, Rongshan Wang, Yanli Wang, Xitao Wang, Guanghai Bai, Nucl. Eng. Technol. 47 (2015) 323–331.
[37] Y. Idrees, Z. Yao, M.A. Kirk, M.R. Daymond, J. Nucl. Mater. 433 (2013) 95–107.
[38] N. Ni, S. Lozano-Perez, J.M. Sykes, G.D.W. Smith, C.R.M. Governor, Corr. Sci. 53 (2011) 4073–4083.
[39] M. Parise, O. Sicardy, G. Cailletaud, J. Nucl. Mater. 256 (1998) 35.
[40] P. Bossis, F. Lefebvre, P. Barbéris, A. Galerie, Mater. Sci. Forum 369–372 (2001) 255.
[41] P. Platt, P. Frankel, M. Gass, M. Preuss, J. Nucl. Mater. 464 (2015) 313–319.
[42] M. Cournil, G. Thomas, J. Chim. Phys. 74 (1977) 545–551.
[43] M. Tupin, M. Pijolat, F. Valdivieso, M. Soustelle, A. Frichet, P. Barberis, J. Nucl. Mater. 317 (2003) 130–144.
[44] G. Zumpicchiat, S. Pascal, M. Tupin, C. Berdin-Méric, Corros. Sci. 100 (2015) 209–221.
[45] K. Colas, R. Verlet, M. Tupin, Zhonghou Cai, K. Wolski, K. Colas, M. Jublot, P. Bossis, Microstructure evolution in ion-irradiated oxidized Zircaloy-4 studied with synchrotron radiation micro-diffraction and transmission electron microscopy, Zirconium in the Nuclear Industry, 18th International Symposium, ASTM STP1597, 2018, pp. 385–414, , http://dx.doi.org/10.1520/STP159720160115.
[46] M. Jublot, G. Zumpicchiat, M. Tupin, S. Pascal, C. Berdin, C. Bisor, M. Blat, Influence of the hydride precipitation on the corrosion kinetics of Zircaloy-4: Effect of the nanostructure and grain boundaries properties of zirconium oxide layer on the oxygen diffusion flux, Zirconium in the Nuclear Industry, 18th International Symposium, ASTMSTP1597, 2018, pp. 350–384, , http://dx.doi.org/10.1520/STP159720160073.